THE MECHANISM OF THERMAL ACCRETION (MUSHROOM) FORMATION AND THE BUBBLE AND FLOW CHARACTERISTICS DURING COLD GAS INJECTION

M. Iguchi,[1] H. Tokunaga,[2] H. Tatemichi[2] and Z. Morita[1]

[1]Faculty of Engineering, Osaka University, 2-1 Yamada-oka, Suita, Osaka 565, Japan
[2]Kakogawa Works, Kobe Steel Ltd, 1 Kanazawa, Kakogawa, Hyogo 675-01, Japan

Abstract—The thermal accretion (or *mushroom*) which is formed around the tuyere in steelmaking plants was simulated by a cold model and its formation process was observed. Single- and multi-hole nozzles were used for gas injection. The multi-hole nozzle was an artificial mushroom-like nozzle. The bubble and flow characteristics were investigated using an electrical resistivity probe and the laser Doppler velocimeter system. The process of thermal accretion formation consists of the following three stages: (1) generation of a core; (2) separation of the core and regeneration of another core; and (3) steady growth of the accretion. The shape of the thermal accretion and the bubble characteristics changed with each stage, depending on the thermal conductivity of the material of the nozzle. The bubble and liquid flow characteristics for the multi-hole nozzle were examined in comparison with those for the single-hole nozzle. The following results were obtained: (1) the bubbling jet generated by the multi-hole nozzle spread more widely in the radial direction than that generated by the single-hole nozzle; and (2) the circulation flow rate for the former nozzle was 33% larger than that for the latter nozzle.

Key Words: injection metallurgy, bubble characteristics, gas holdup, thermal accretion

1. INTRODUCTION

In steelmaking processes, bottom gas blowing is a method widely utilized to agitate molten iron and to accelerate refining rates. In actual steelmaking operations, a mushroom- or cone-shaped porous lump of solid iron is formed (Boxall *et al.* 1982; Ohguchi & Robertson 1983; Tanaka *et al.* 1982) around the tuyere at the bottom of the vessel. Mushroom formation significantly prolongs the life of the tuyere and the brickwork around the tuyere (Guthrie 1989). In this research, the following three subjects were dealt with using a cold model:

(1) Observation of the thermal accretion formation process.
(2) An analysis of the effects of the thermal conductivity of the nozzle materials on the formation of the thermal accretion.
(3) A comparison of the results of the bubble and flow characteristic studies for the multi-hole nozzle with previous data for the single-hole nozzle.

2. EXPERIMENT

2.1. Experimental apparatus

Figure 1 shows a schematic diagram of the experimental apparatus. Compressed air was fed to a heat exchanger through a dehumidifier (which prevents both a decrease in the heat transfer rate and choking due to frosting), a regulator and a mass flowmeter. The air was cooled to $-185°C$ by the heat exchanger filled with liquid nitrogen. The temperature of the cooled air was controlled by a bypass valve and the air was blown into water in a cylindrical vessel through a nozzle located at the center of the bottom plate. It is well-known that the gas-to-liquid density ratio ρ_G/ρ_L has a significant effect on the flow near the nozzle exit (Iguchi *et al.* 1992a), and helium or hydrogen is usually used as the gas and water as the liquid to simulate gas injection into an iron bath. The main purpose of the present study is to clarify the effect of the nozzle material on the formation of thermal accretion, and air was used as an injection gas because it is easy to handle. The ρ_G/ρ_L
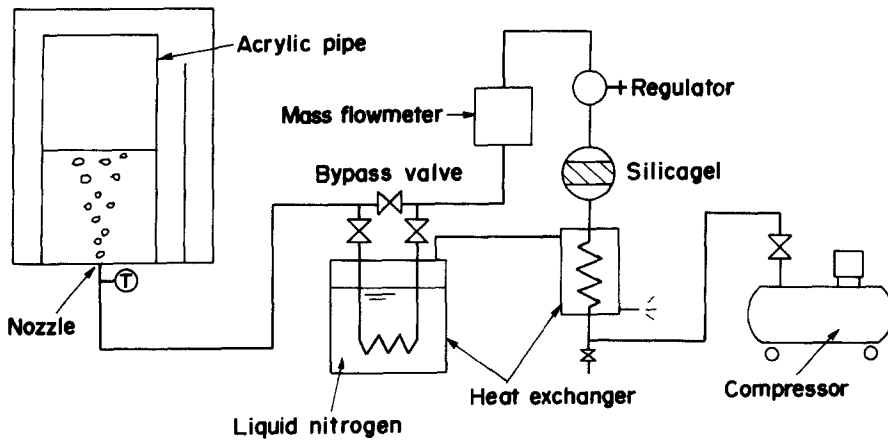
Figure 1. Experimental apparatus.

value of the model, therefore, became much larger than that in industrial practice. Although the density ratio ρ_G/ρ_L is considered to be less influential in the formation of thermal accretion than the thermal properties of the gas and liquid, details of the effect of ρ_G/ρ_L must be left for a future study.

The gas pipe and the shell of the heat exchanger were thermally insulated with polyethylene foam. The vessel used for the experiments on thermal accretion formation and bubble characteristics was made of acrylic resin and had an inner diameter of 200 mm and a height of 400 mm. For the experiments on liquid flow characteristics, the acrylic vessel had an inner diameter of 126 mm and a height of 252 mm. A bubbling jet in a cylindrical bath subject to centric bottom gas injection rotates around the vessel axis under a certain blowing condition. Such swirl motions
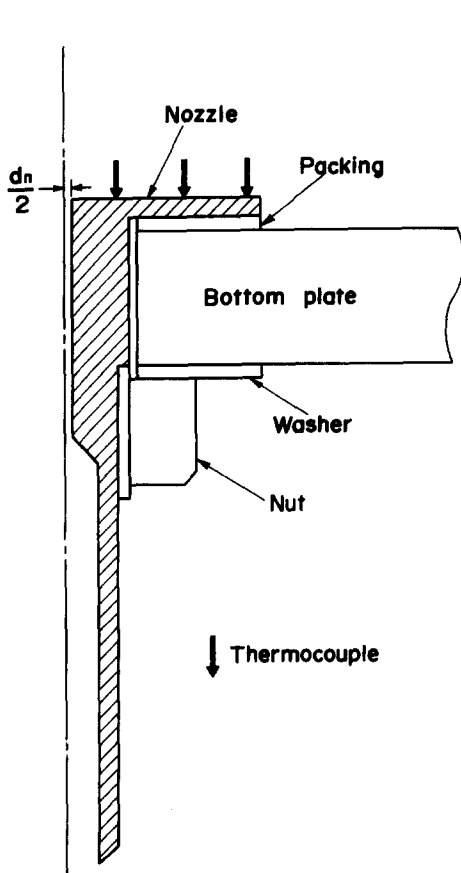

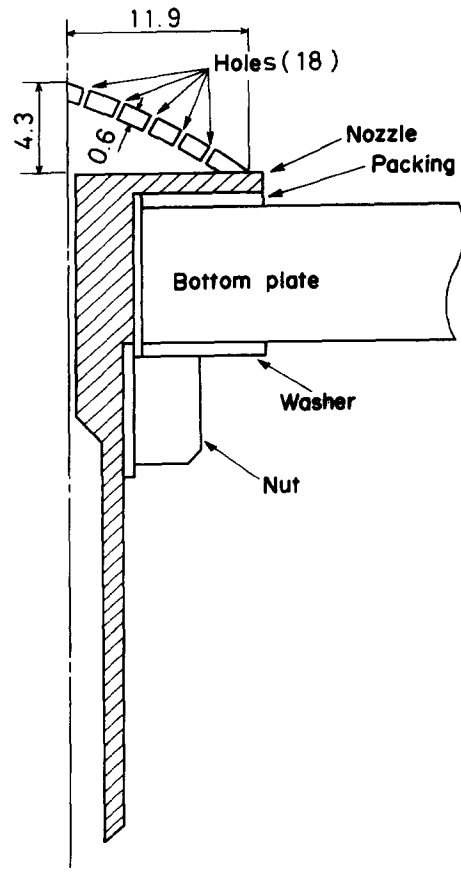Figure 2. Schematic illustration of a single-hole nozzle.

Figure 3. Schematic illustration of a multi-hole nozzle.

of a bubbling jet can be classified into two types. The conditions describing the occurrence and cessation of these swirl motions have been presented elsewhere (Iguchi *et al.* 1992b). Since the bubble and liquid flow characteristics under the swirl motion were complicated, the present experiment was performed for a bubbling jet rising directly upwards.

Figure 2 shows a schematic illustration of a single-hole nozzle. Although the injection tuyere consists of an annular pipe under the actual operating condition of the LD converter, a single-hole nozzle was employed in order to determine the effect of the thermal conductivity of the nozzle material on the thermal accretion formation process. Two kinds of nozzle materials were used, brass and acrylic resin. Both types of nozzles had an inner diameter of 1 mm. To measure the temperature on the nozzle surface, three thermocouples (chromel–alumel, ϕ 0.5 mm) were installed at $r = 4$, 9 and 14 mm, where r is the radial distance from the nozzle center. These thermocouples were buried into grooves on the nozzle surface; the grooves having a depth of 0.5 mm. Thermocouples were fixed with solder for the case of the brass nozzle, and with acrylic resin for the case of the acrylic nozzle.

2.2. Temperature measurements for the injected air and water in the bath

The temperature of the air injected into the bath was measured by a thermocouple (chromel–alumel, ϕ 1.5 mm) installed in the nozzle near the exit. The temperature of the bath water was measured using three thermocouples (chromel–alumel, ϕ 1.5 mm) located in the upper, middle and lower parts of the bath, respectively.

2.3. Observation of the thermal accretion formation

In order to simulate the thermal accretion, cold air, at a temperature between -110 and $-130°C$, was injected into water at an initial temperature of $30°C$. The actual volumetric flow rate of the air was 168.3 cm³/s. The temperature of the injected air and that on the nozzle surface were measured at 5 s intervals. To enhance the cooling rate of the bath water crushed ice was added gradually to the bath.

2.4. Measurement of bubble characteristics

Since it is difficult to maintain a thermal accretion without changing its shape and size, the thermal accretion was further modeled, using a hemispherical multi-hole nozzle made of a plastic ball (figure 3). The shape and size of the nozzle, and the number, diameter and distribution of the holes were modeled on the basis of the observation of the simulated thermal accretion.

The bubble characteristics, i.e. gas holdup (void fraction) ϵ, bubble frequency f_B, mean bubble rise velocity $\bar{u}_B$ and mean bubble chord length $\bar{L}_B$, were measured with a double-sensored electrical resistivity probe for gas injection at ambient temperature. The temperatures of the injection gas and bath were $25°C$. The electrical resistivity probe has two electrode tips made of copper wire of 0.1 mm diameter. The vertical distance between the two electrode tips was set to be 1.5 mm. Each electrode was insulated with acrylic resin except at its tip. The probe signals were digitized at a
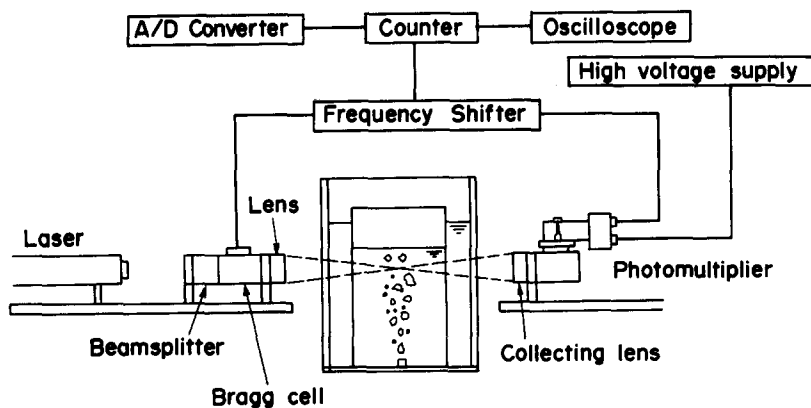

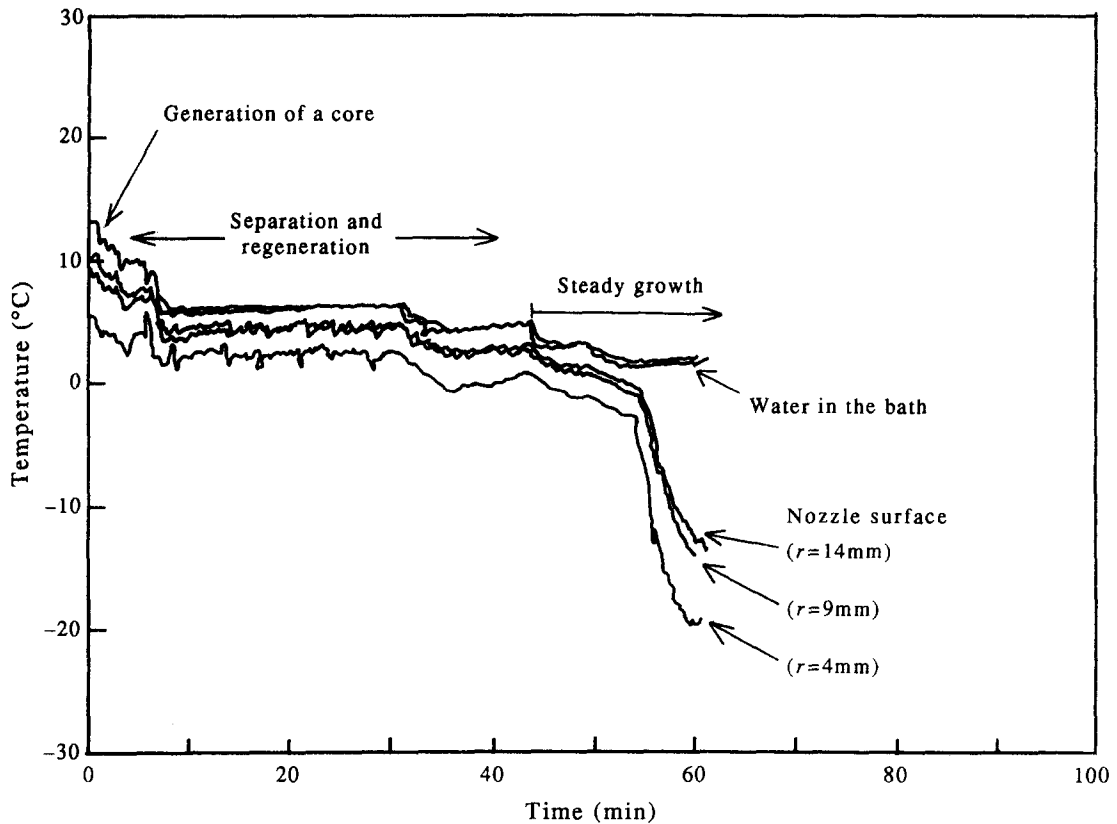Figure 4. LDV system used for the measurement of liquid velocity.

Figure 5. Temperature change during thermal accretion growth (brass nozzle).

sampling frequency of 5 kHz. 1.5×10^5 digitized signal data were processed to obtain the bubble frequency f_B and the gas holdup ϵ. Furthermore, a total of 2400 bubble signals were stored to obtain the mean bubble rise velocity $\bar{u}_B$ and the mean bubble chord length $\bar{L}_B$.

2.5. Measurement of liquid flow characteristics

For the measurement of liquid velocity, the laser Doppler velocimeter (LDV) system was employed (figure 4). The test vessel was settled in another square vessel and filled with water both inside and outside the test vessel in order to decrease the effect of refraction due to the curved wall. In addition, traversing equipment was used to make it possible to move the LDV probe three-dimensionally. A/D-converted output signals of the LDV, which involved hold signals, were processed by a personal computer every 500 μs under the present experimental condition. If the LDV signal kept a constant value for over 500 μs, these signals except the first one were regarded as the hold signal and eliminated. However, the remaining data involved the signals of the bubble surface. These signals also were removed using the output signal of an electrical resistivity probe, whose electrode tip was placed just above the measurement point, i.e. the intersection of two laser beams. The rate of velocity signals of the bubble surface was $\lesssim 3\%$ even for a gas holdup value of 30%, and these signals had a negligible effect on $\bar{u}$ and $u'_{r.m.s.}$, although the Reynolds shear stress was

---

(Figures 6–10 Opposite)

Figure 6. The appearance of bubble formation when the frozen core was formed (brass nozzle).

Figure 7. The bubble formation when steady core growth began (brass nozzle).

Figure 8. The bubble formation during continuing steady growth (brass nozzle).

Figure 9. Simulated thermal accretion (acrylic nozzle).

Figure 10. The appearance of bubble formation for the single-hole nozzle.
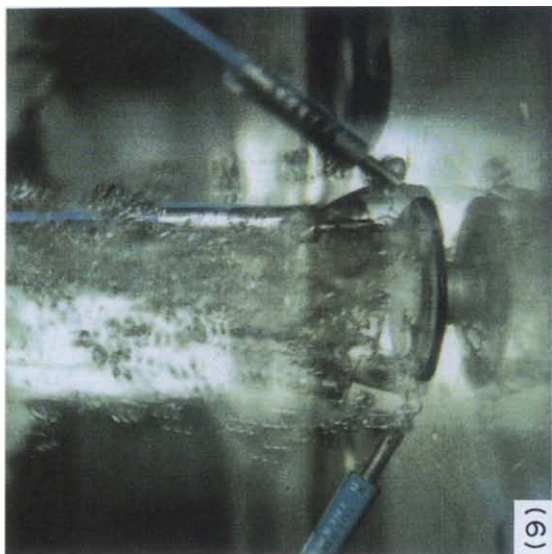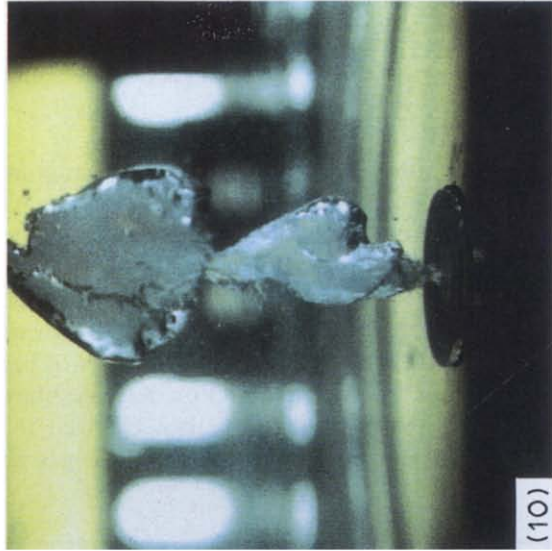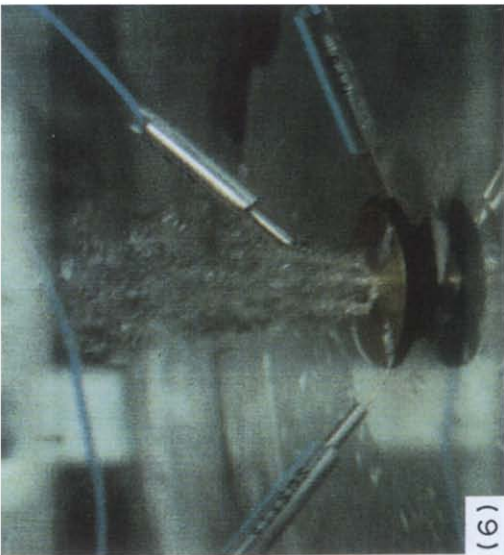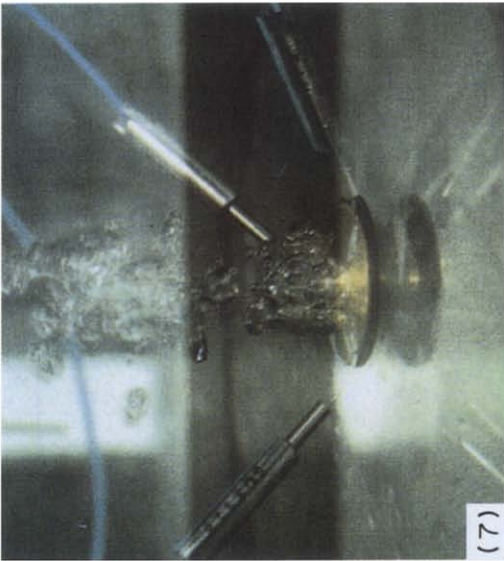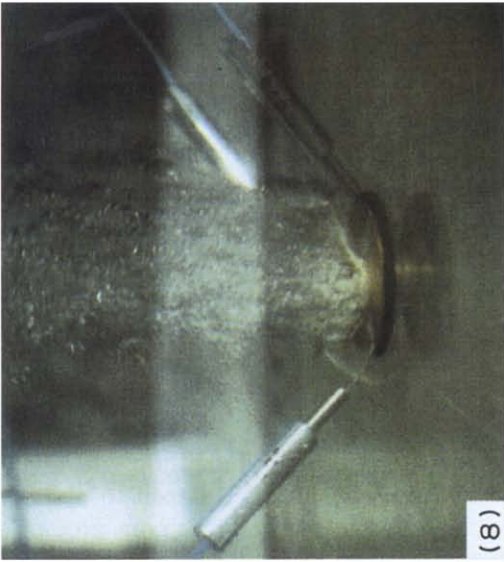
Figures 6–10. *Captions at foot of p. 176.*

affected significantly by them. More than 5000 data points were processed to obtain the axial mean velocity $\bar{u}$ and the root-mean-square (r.m.s.) value of the axial turbulence component $u'_{\text{r.m.s.}}$:

$$\bar{u} = \sum_{i=1}^{N} u_i / N \tag{1}$$

and

$$u'_{\text{r.m.s.}} = \left[\sum_{i=1}^{N} (u_i - \bar{u})^2 / N \right]^{1/2} \tag{2}$$

The radial mean velocity $\bar{v}$ and the r.m.s. value of the radial turbulence component $v'_{\text{r.m.s.}}$ were obtained in the same way. The sampling time at each measurement location was about 30 min. A small amount of white pigment was used to form scattering particles.

3. EXPERIMENTAL RESULTS AND DISCUSSION

3.1. Thermal accretion formation

Figure 5 shows the measured temperature change at each measurement position during thermal accretion growth in the case of the brass nozzle. As the water temperature dropped to about 14°C, a frozen ice core was formed near the nozzle hole (figure 6). This frozen core grew around the jet but separated from the nozzle after a while. Then another core was formed. This sequence of events was repeated several times. When the water temperature dropped to about 7°C, the frozen core no longer separated and steady core growth began (figures 7 and 8). The temperature on the nozzle surface at which steady core growth began was about 0°C. The temperature of the nozzle underneath the thermal accretion decreased further with time. At the initial stage, the shape of the core was like a mushroom, then changed to conical and finally became hemispherical. When it became hemispherical, the paths of the gas were clearly observable (figure 9). The bubble
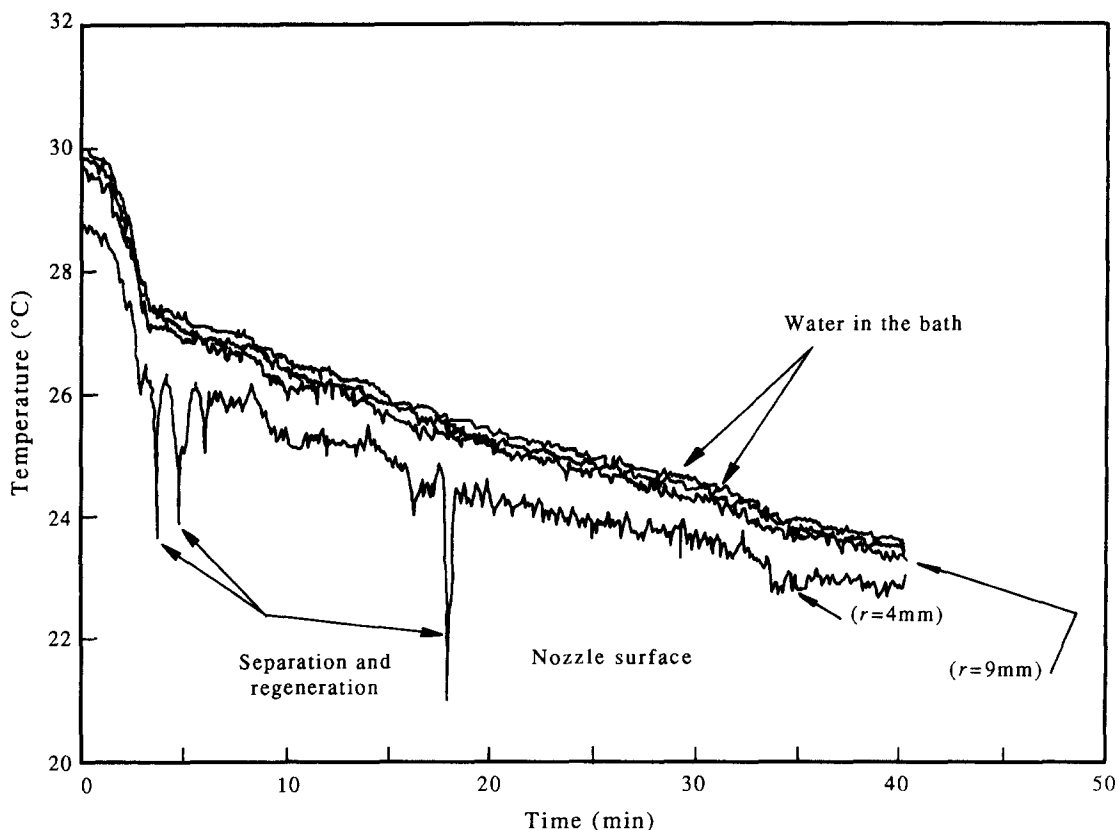

Figure 11. Temperature change during the generation of the frozen core (acrylic nozzle).
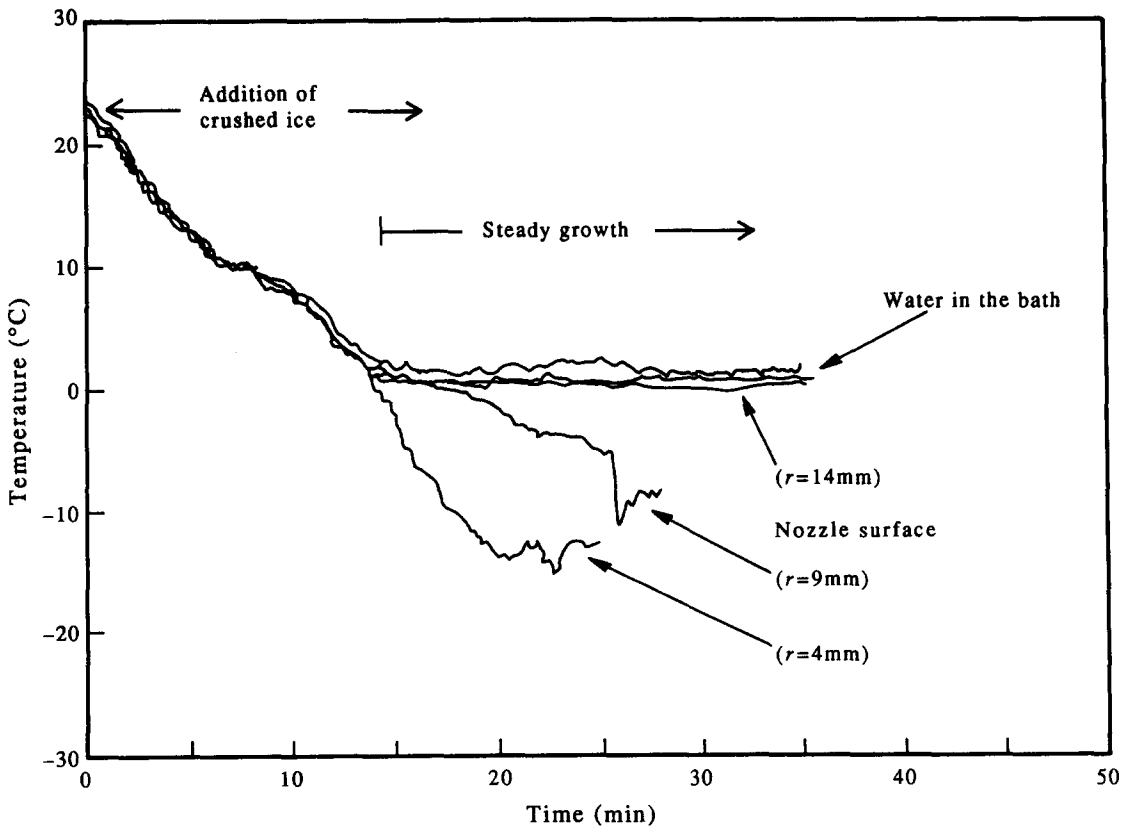
Figure 12. Temperature change during thermal accretion growth (acrylic nozzle).

formations at the nozzle before and after the frozen core formation were quite different from each other (figures 9 and 10). During the growth of the steady frozen core, the bubble formation was similar to that with a multi-hole nozzle.

Figures 11 and 12 show the temperature change at each measurement position during the thermal accretion growth in the case of the acrylic nozzle. A frozen core first appeared at a bath temperature of about 27°C. However, the water temperature at which the frozen core started to grow steadily
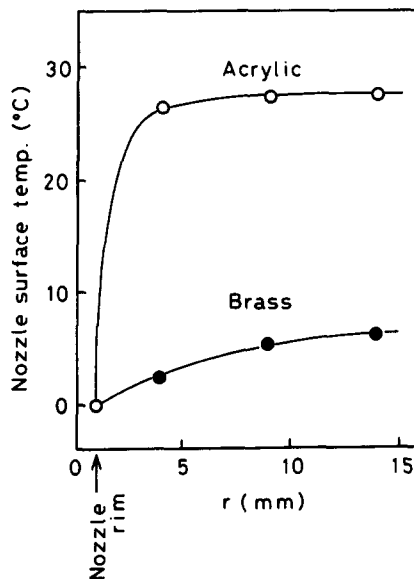

Figure 13. Radial distribution of temperature on the nozzle surface.

was about 0°C. Figure 13 shows the radial temperature distributions at the instant the frozen core was created. At that time, the temperature of the rim of nozzle exit was about 0°C. The same is true for the brass nozzle. Therefore, in the area of $r \leqslant 4$ mm the radial temperature gradient was higher for the acrylic nozzle. Such a radial temperature gradient difference caused the subsequent growth behavior of the thermal accretion. The thermal accretion kept its hemispherical shape as it grew. The appearances of the thermal accretion for both the brass and acrylic nozzles are summarized in figure 14.

In order to differentiate between the temperature distributions on the surface of the brass and acrylic nozzles the instant when the frozen core is no longer separated, a numerical analysis of the time-dependent heat conduction was made using the finite difference method (JSME 1986). The domain for the analysis is indicated by the thick solid line in figure 15. As for the boundary conditions, the heat transfer coefficients on the nozzle surface and inside the nozzle were evaluated following Katagiri et al. (1987). The remaining walls were assumed to be adiabatic. The temperature of the water was assumed to be 7°C for the brass nozzle and 27°C for the acrylic nozzle. As an initial condition, the temperature of the domain under analysis was assumed to be uniform and equal to the abovementioned water temperature. The computation was stopped when the temperature of the nozzle rim became 0°C. The computation time was about 85 s for the brass nozzle and about 5 s for the acrylic nozzle. Although the temperature of the nozzle rim was 0°C for both cases, the surface temperatures of the two types of nozzle differed from each other due to the difference in the thermal conductivity. Therefore, it can be considered that the shape of the thermal accretion during the initial stage of its growth is strongly dependent on the thermal conductivity of the nozzle material.

The reason why the shape of the accretion during the final stage was similar, i.e. hemispherical, in both cases can be explained as follows. As the diameter of the thermal accretion exceeded the outer diameter of the nozzle, the effect of the thermal conductivity of the nozzle material became relatively small, because the bottom plate is acrylic for both cases.
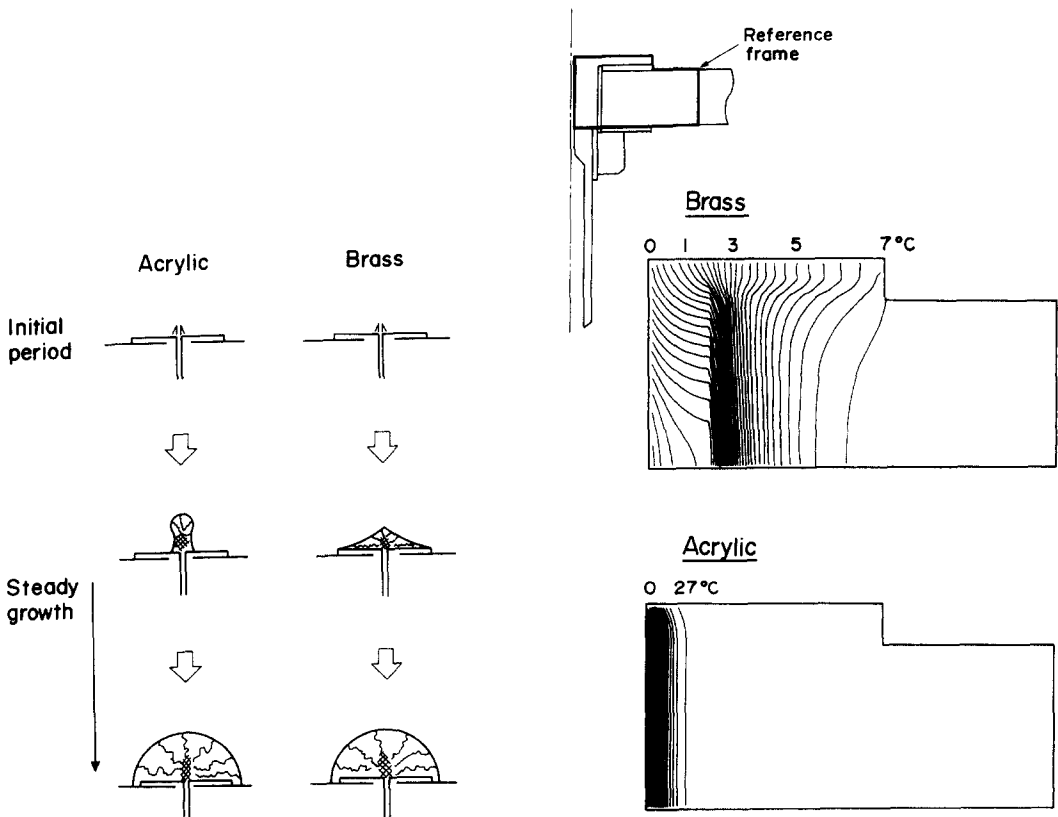

Figure 14. Appearance of the thermal accretion for a brass nozzle and an acrylic nozzle.

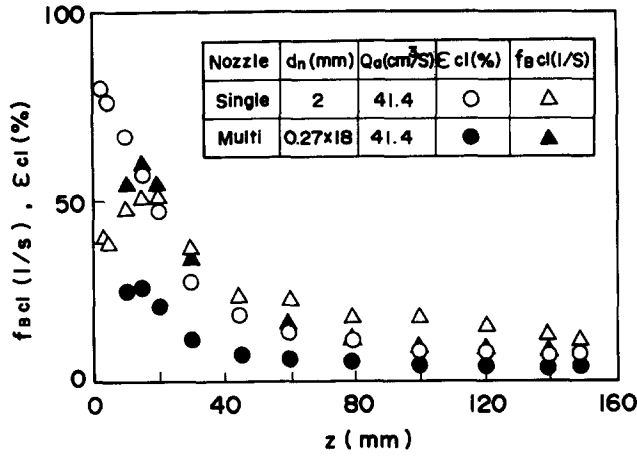Figure 15. Results of the numerical analysis of temperature distributions.

Figure 16. Axial distributions of bubble frequency $f_{B,cl}$ and gas holdup ϵ_{cl} on the centerline.

The results obtained from the observation of the thermal accretion can be summarized as follows:

(1) The thermal accretion formation process consists of the following three stages: (a) generation of an ice core; (b) separation of the core and regeneration of another core; and (c) steady growth.

(2) The thermal accretion starts to grow when the temperature of the nozzle surface reaches the solidification tememperature of the liquid. The shape of the thermal accretion depends on the thermal conductivity of the nozzle materials until the outer edge of the thermal accretion reaches the outer edge of the nozzle.

3.2. Bubble characteristics

Figure 16 shows the axial distributions of the bubble frequency $f_{B,cl}$ and the gas holdup ϵ_{cl} on the centerline. The experimental conditions are given in the figure; Q_a represents the actual volumetric gas flow rate. The bubble frequency $f_{B,cl}$ in the region near the nozzle is an increasing function of the number of nozzle holes, but above $z = 25$ mm the reverse tendency was observed. The measured value of the gas holdup ϵ_{cl} for the multi-hole nozzle was smaller everywhere than that for the single-hole nozzle. This tendency was particularly notable near the nozzle.

Figures 17 and 18 show the radial distributions of the bubble frequency f_B and the gas holdup ϵ at $z = 30$ mm. It is clear that the distributions of f_B and ϵ for the multi-hole nozzle spread wider in the radial direction than for the single-hole nozzle. In particular, the total number of bubbles obtained by integrating f_B over the bubbling jet cross section, becomes large as the number of nozzle holes increases.
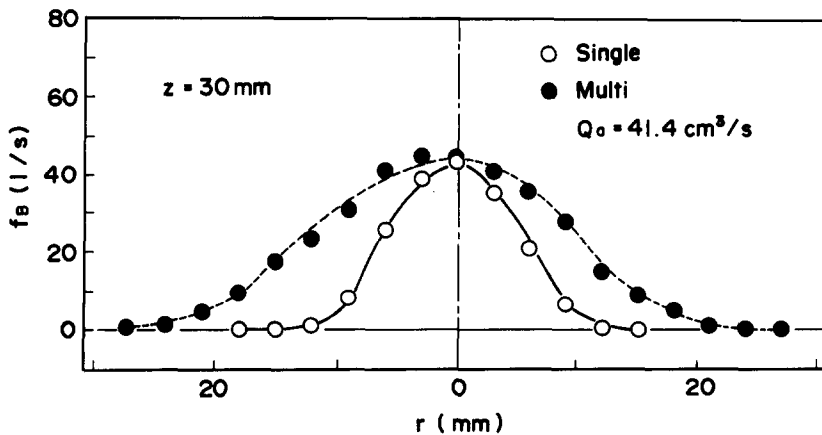

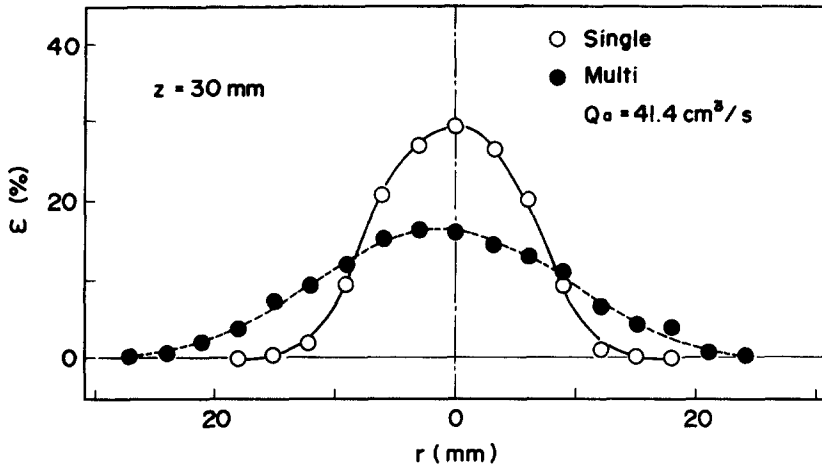Figure 17. Radial distributions of bubble frequency f_B at $z = 30$ mm.

Figure 18. Radial distribution of gas holdup ϵ at $z = 30$ mm.

Figures 19 and 20 show the radial distributions of the bubble frequency f_B and the gas holdup ϵ at $z = 80$ mm. The value of f_B for the multi-hole nozzle was larger everywhere than that for the single-hole nozzle. This fact indicates that the bubble size is a decreasing function of the number of nozzle holes. For the single-hole nozzle, it is well-known that the radial distributions of f_B and ϵ fall within the Gaussian distribution. Also, for the multi-hole nozzle, these distributions obeyed the Gaussian distribution well.

Figures 21 and 22 show the radial distribution of the mean bubble rise velocity $\bar{u}_B$ at $z = 30$ mm and $z = 80$ mm. In the region near the nozzle ($z = 30$ mm), the multi-hole nozzle induced a smaller value of $\bar{u}_B$ than the single-hole nozzle. This may be caused by the difference in the inertia forces of the injected gas between the two nozzles. In the region far from the nozzle ($z = 80$ mm) the difference was very small, because only the buoyancy force of the bubbles plays an important role at this location.

3.3. Liquid flow characteristics

Figure 23 shows the distribution of the mean axial velocity $\bar{u}_{cl}$ and the r.m.s value of the axial turbulence component $u'_{r.m.s.,cl}$ on the centerline. In the region near the nozzle, $\bar{u}_{cl}$ becomes smaller as the number of nozzle holes increases. This tendency agrees with that for the bubble rise velocity measured with the electrical resistivity probe. Under the present experimental condition, the region $z \lesssim 70$ mm belongs to the momentum region in which the inertia force of the injection gas is surpassed, and the region $z \gtrsim 70$ mm belongs to the buoyancy region in which the buoyancy force
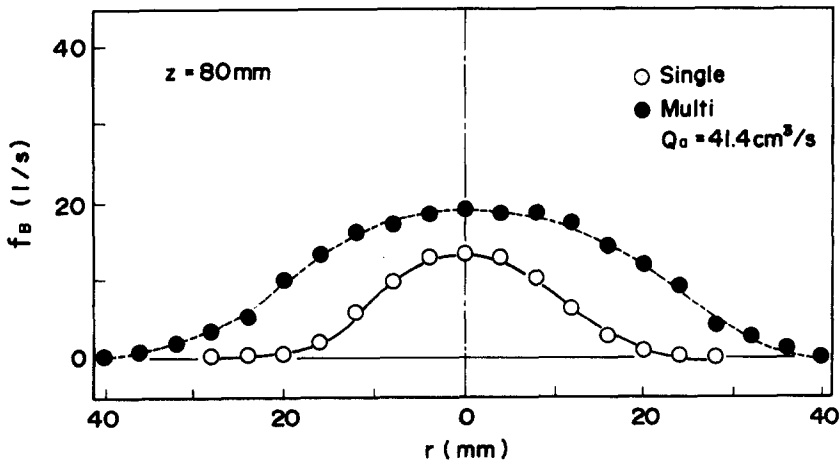

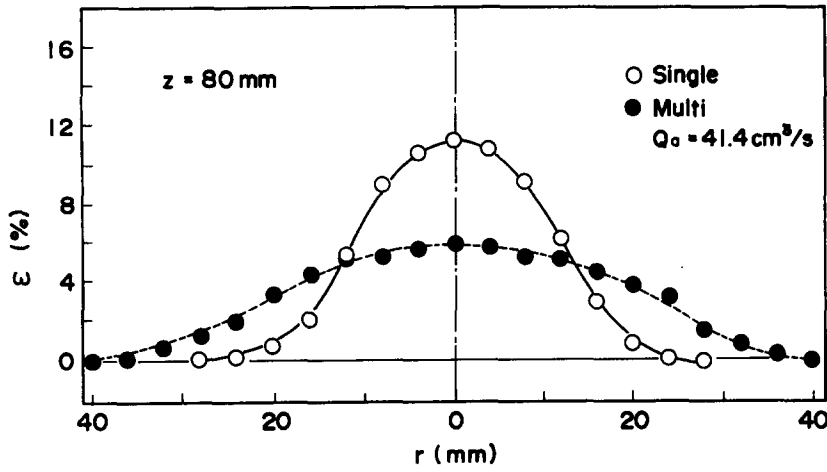Figure 19. Radial distributions of bubble frequency f_B at $z = 80$ mm.

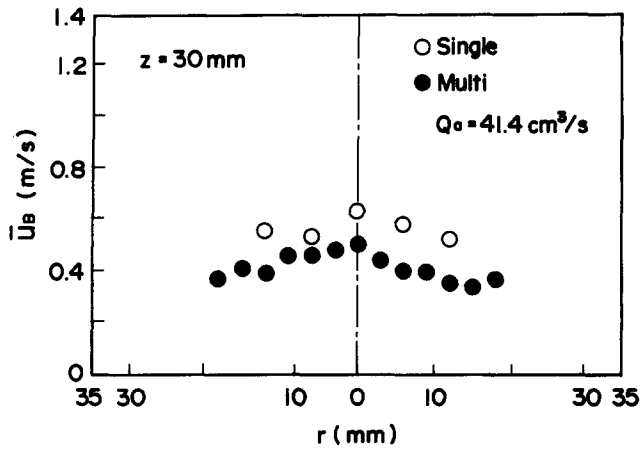Figure 20. Radial distributions of gas holdup ϵ at $z = 80$ mm.

Figure 21. Radial distribution of the mean bubble rise velocity $\bar{u}_B$ at $z = 30$ mm.
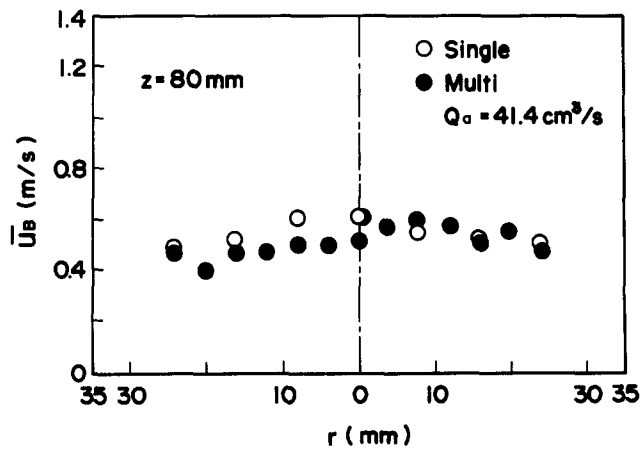

Figure 22. Radial distribution of the mean bubble rise velocity $\bar{u}_B$ at $z = 80$ mm.
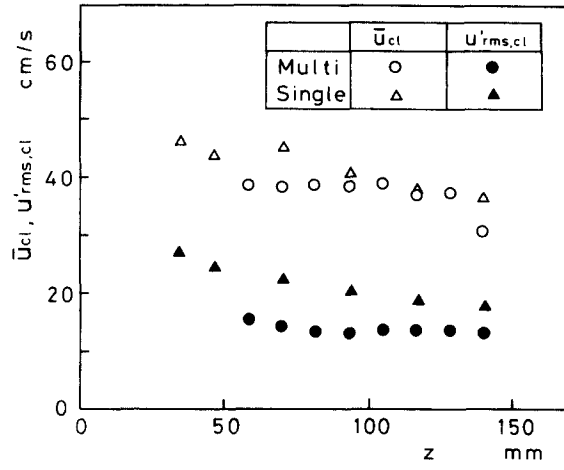
Figure 23. Axial distributions of the mean axial velocity $\bar{u}_{cl}$ and the r.m.s. value of the axial turbulence component $u'_{r.m.s.,cl}$ on the centerline.
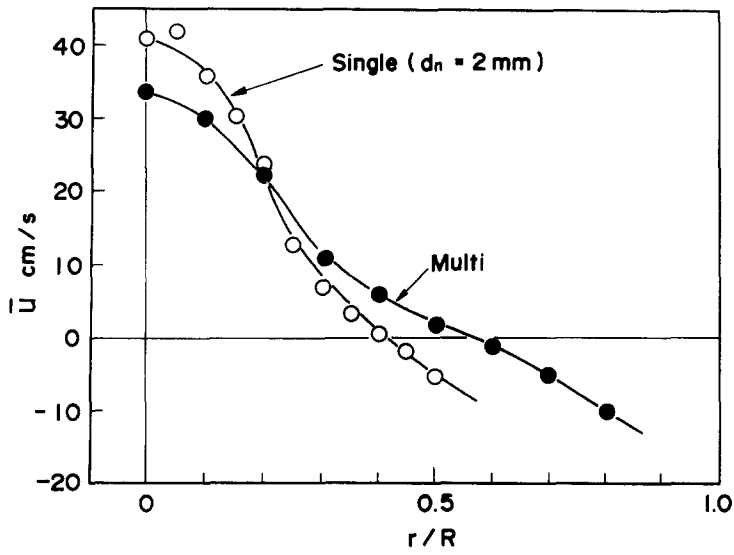

Figure 24. Radial distributions of the axial mean velocity $\bar{u}$ at $z = 93.2$ mm.
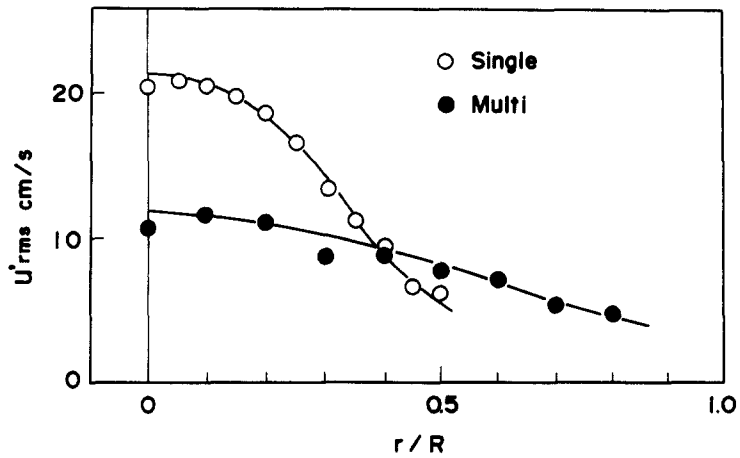

Figure 25. The r.m.s. value of the axial turbulence component $u'_{r.m.s.}$ at $z = 93.2$ mm.

of the bubbles plays a dominant role (Iguchi *et al.* 1991). The r.m.s. value of the axial turbulence component was smaller than that for the single-hole nozzle and kept a constant value in the axial direction. In the case of the single-hole nozzle, the turbulence intensity T_u ($=u'_{r.m.s.,cl}/\bar{u}$) was about 40–50%, but for the multi-hole nozzle it ranged from 30 to 40%. The difference may be attributable to the fact that bubbles generated by the multi-hole nozzle are only moved by the buoyancy force, whereas bubbles generated by the single-hole nozzle are moved by both the buoyancy and inertia forces.

Figures 24 and 25 show the radial distributions of the axial mean velocity $\bar{u}$ and the r.m.s. value of the axial turbulence component $u'_{r.m.s.}$, respectively, at $z = 93.2$ mm. Near the centerline, the axial mean velocity $\bar{u}$ for the multi-hole nozzle was smaller, but the width of the upward flow region was larger than for the single-hole nozzle. These results agree with those for the gas holdup ϵ. The rate of the circulation flow driven by bubbles can be obtained by integrating the radial distribution of the axial mean velocity directed upwards. The circulation flow rate for the multi-hole nozzle was 33% larger than that for the single-hole nozzle.

The multi-hole nozzle brings about a smaller r.m.s. value of the axial turbulence component near the centerline than the single-hole nozzle.

4. SUMMARY AND CONCLUSIONS

The main findings of this study can be summarized as follows.

4.1. Thermal accretion formation

The thermal accretion formation was modeled by a cold model experiment. The thermal accretion formation process consisted of three stages: (1) the generation of an ice core; (2) the separation of the core and regeneration of another core; and (3) steady continuing growth. The shape of the thermal accretion depended strongly on the thermal conductivity of the nozzle material until the outer edge of the accretion reached the outer edge of the nozzle.

4.2. Bubble behavior

(1) The bubble size changed drastically before and after the thermal accretion formation. The bubble behavior characterized by ϵ, f_B and $\bar{u}_B$ depended on the shape of the thermal accretion and hence changed at each stage of growth of the thermal accretion. The bubbling jet spread wider as the thermal accretion grew.

(2) Since it was difficult to maintain a thermal accretion without changing its size and shape, the thermal accretion was modeled further by a multi-hole nozzle. The bubble behavior for the multi-hole nozzle was compared with that for a single-hole nozzle. The bubble frequency on the centerline $f_{B,cl}$ for the multi-hole nozzle was larger than that for the single-hole nozzle near the nozzle exit, but in the region far from the nozzle, the tendency was reversed. The gas holdup on the centerline ϵ_{cl} for the multi-hole nozzle was smaller everywhere than that for the single-hole nozzle. The radial distributions of both the bubble frequency and gas holdup for the multi-hole nozzle spread wider in the radial direction than those for the single-hole nozzle. The mean bubble rise velocity $\bar{u}_B$ for the multi-hole nozzle showed a smaller value than that for the single-hole nozzle in the region near the nozzle, but the difference became small as the axial distance from the nozzle increased.

4.3. Liquid flow behavior

(1) The multi-hole nozzle induced a smaller axial mean velocity $\bar{u}$ near the centerline but a wider upward flowing region compared with the single-hole nozzle. The circulation flow rate for the multi-hole nozzle was about 33% larger than that for the single-hole nozzle.

(2) In the bubbling jet region where bubbles and liquid coexist, the turbulence intensity T_u for the multi-hole nozzle became much smaller than that for the single-hole nozzle.

The present study hopefully provides a deeper understanding of the shape and formation mechanism of the thermal accretion in the tuyere; in particular, it also clarifies how this accretion affects the conditions for bottom gas blowing.

REFERENCES

BOXALL, G., SABHARWAL, A. K., ROBERTSON, T., & HAWKINS, R. J. 1982 Injection phenomena in extraction and refining. Report B1-18, Univ. of Newcastle-upon-Tyne, U.K.

GUTHRIE, R. I. L. 1989 *Engineering in Process Metallurgy*, pp. 301–303. Clarendon Press, Oxford.

IGUCHI, M., NOZAWA, K. & MORITA, Z. 1991 Bubble characteristics in the momentum region of air–water vertical bubbling jets. *ISIJ Int.* **31**, 952–959.

IGUCHI, M., DEMOTO, Y., SUGAWARA, N. & MORITA, Z. 1992a Behavior of an Hg–air vertical bubbling jet in a cylindrical vessel. *Tetsu-to-Hagane* **78**, 407–414.

IGUCHI, M., HOSOHAR, S., KOGA, T., YAMAGUCHI, R. & MORITA, Z. 1992b The swirl motion of a vertical bubbling jet in a cylindrical vessel. *Tetsu-to-Hagane* **78**, 1778–1785.

JSME 1986 *JSME Data Book: Heat Transfer*, 4th edn, pp. 16–26. JSME, Tokyo.

KATAGIRI, S., OZAWA, Y., MORI, K. & SANO, M. 1987 Tuyere accretion growth at gas injection into liquid. *Tetsu-to-Hagane* **73**, 2206–2213.

KISHIMOTO, Y., KATO, Y., FUJII, T. & KAKIOI, Y. 1984 The formation mechanism of solid iron rump around the bottom gas blowing tuyere of the converter. *Tetsu-to-Hagane* **70**, S254.

NAKAMURA, H., SAITO, K., NOSAKI, T., SUZUKI, K., OHNUMA, K. & EMI, T. 1981 Solid iron rump around the tuyere of the converter. *Tetsu-to-Hagane* **67**, S873.

OHGUCHI, S. & ROBERTSON, D. G. C. 1983 Formation of porous accretions around the tuyere during gas injection. *Ironmaking Steelmaking* **10**, 15–23.

TANAKA, S., OHKOHIRA, K., HIRAI, M. & ABE, S. 1982 Study on mushroom formation and nature using a small model. *Tetsu-to-Hagane* **68**, S889.

XU, C., SAHAI, Y. & GUTHRIE, R. I. L. 1984 Formation of thermal accretions in submerged gas injection process. *Ironmaking Steelmaking* **11**, 101–107.